Available online at www.sciencedirect.com
SCIENCE DIRECT®
Catalysis Today 98 (2004) 387–392
CATALYSIS TODAY
www.elsevier.com/locate/cattod

Novel nanocrystalline Ga–Al–Zn complex oxide: catalyst for simultaneous treatment of NPAC and lean NO_x

S.C. Shen, K. Hidajat, L.E. Yu, S. Kawi*

Department of Chemical and Biomolecular Engineering, National University of Singapore, 4 Engineering Drive 4 117576, Singapore

Available online 5 November 2004

Abstract

Nanocrystalline Ga–Al–Zn complex-oxide (designated here as nano-GAZ) has been successfully synthesized using hydrothermal method. Using TEM, BET, FTIR, DTA–TGA, and XRD, synthesized nano-GAZ particles are shown as high-surface-area nanoparticles comprising typical spinel crystal structures. The nano-GAZ catalyst was tested as a new deNPAC catalyst, using pyridine as the model NPAC compound. The reaction results show that pyridine could be completely oxidized over nano-GAZ catalyst above 400 °C. Furthermore, NO formation was significantly decreased due to the excellent performance of the nano-GAZ catalyst for the selective catalytic reduction of NO_x with hydrocarbon in the presence of excess oxygen. An optimal reaction temperature at around 440–500 °C was observed to achieve complete catalytic oxidation of pyridine with the lowest NO_x formation. These results demonstrate a promising approach for dual-mitigation of NPAC and NO_x pollutants using nano-GAZ catalyst.

Keywords: Nanocrystalline; Complex-oxide; DeNPAC; $DeNO_x$; Environmental catalysis

1. Introduction

N-containing polycyclic aromatic compounds (NPACs) present in diesel-engine emissions are known to be carcinogenic. Many kinds of NPACs – such as nitropyrene, nitronaphthalene, nitrobiphenyl, nitrofluorene, nitrophenanthrene, nitroanthracene, and nitrofluoranthene – have been found in diesel exhaust [1]. The concentration of NPACs in diesel exhaust is dependent on the fuel type, engine type and the engine working conditions. For instance, the concentration of 1-nitropyrene, which is the most abundant NPACs in diesel emission extracts, is currently in the range of 0–10 ppm. To meet the increasing demand of air quality and environmental protection, it is of great importance to remove NPACs from the diesel emission. However, direct pyrolysis of NPACs generates substantial NO_x emissions, as most of the nitrogen in NPACs will be oxidized to NO_x [2]. Hence, an effective catalyst for catalytic oxidative decomposition of NPAC is desired.

Catalytic decomposition of NPACs, using pyridine as the model NPAC compound, had been carried out in the past on Pt, $CuCr_2O_4$, $NiCr_2O_4$, and CuO supported on γ-Al_2O_3 [3–5]. It was found that at temperatures between 240 and 550 °C, pyridine could be oxidatively decomposed to CO_2, H_2O, N_2, and NO_x and the yield of NO_x was found to increase with the increase of reaction temperature. Since the control of NO_x emission is a critical subject, especially in the presence of excess oxygen, it is a great challenge to reduce the amount of NPACs in tail-pipe exhausts without causing additional NO_x emission. Ever since Iwamoto et al. [6] reported that Cu-ion-exchanged ZSM-5 catalysts were active for selective catalytic reduction (SCR) of lean NO_x in the presence of excess oxygen, numerous catalysts, such as zeolite-based catalysts [7–11], supported noble metal catalysts [12–15], and metal oxide catalysts [16–18], have been extensively investigated. However, up to date, no such catalysts could be used in real conditions for the SCR of NO_x with hydrocarbons in the presence of excess oxygen. Furthermore, as the combustion of NPACs produces NO_x, it is necessary to search for a viable deNPAC catalyst capable of completely oxidizing NPACs with minimal formation of NO_x. Metal-oxide catalysts, especially in the form of

* Corresponding author.
E-mail address: chekawis@nus.edu.sg (S. Kawi).

0920-5861/$ – see front matter © 2004 Elsevier B.V. All rights reserved.
doi:10.1016/j.cattod.2004.08.014

complex oxides, seem to offer a great potential for practical application – in terms of activity/stability – to control NO_x emission and thus have received extensive attention in environmental catalysis [19–21].

In this paper, we describe the synthesis of a novel nanocrystalline Ga–Al–Zn complex oxide (designated here as nano-GAZ) using hydrothermal synthetic method and the application of the resulting nano-GAZ catalyst for oxidative decomposition of pyridine. The high catalytic activity of the nano-GAZ catalyst for decomposition of pyridine above 400 °C is observed. Since the novel nano-GAZ catalyst shows excellent performance in controlling NO formation at 400–500 °C, it has very great potential to be developed as a practical environmental catalyst for simultaneous abatement of NO_x and NPACs from diesel engine exhausts.

2. Experimental

A typical synthesis of nano-GAZ is as follows: 10.41 g of $Zn(NO_3)_2{\cdot}6H_2O$, 15.36 g of $Al(NO_3)_3{\cdot}9H_2O$ and 10.44 g $Ga(NO_3)_3$ were dissolved in 150 ml of water at room temperature. A desired amount of aqueous ammonia (10%) was added to this mixed solution to control the solution pH at 5–5.5. The mixture was transferred to a teflon vessel held in a stainless steel autoclave. After the vessel was sealed, it was statically placed in a thermostatic oven and heated at 180 °C for 20 h. The solid material was recovered by centrifuging, drying at 80 °C in a vacuum oven overnight, followed by calcination in air at 750 °C for 5 h using a heating rate of 5 °C/min.

A contrasting sample of Ga–Al–Zn complex oxide (having the same composition as the above nano-GAZ) was prepared by simple precipitation (i.e. without any hydrothermal treatment), followed by the same filtration, drying, and calcination procedures as that used in the preparation of nano-GAZ catalyst.

Characterization: TEM images were obtained using a JEOL TEM-2010 instrument at 200 kV. N_2 adsorption–desorption isotherms were measured by nitrogen physisorption at 77 K using an Auto-Sorb 1 Analyzer (Quantachrome). Before nitrogen adsorption–desorption measurements, the sample was outgassed at 300 °C under vacuum for 2 h. The specific surface areas of the samples were determined from the linear portion of the BET plots and the pore size distribution was calculated from the desorption branch of N_2 isotherms using the conventional Barrett-Joyner-Halenda (BJH) method as suggested by Tanev and Vlaev [22].

Powder X-ray diffraction patterns of the samples were recorded using a Shimadzu XRD-6000 powder diffractometer, where Cu target Kα-ray (operating at 40 kV and 30 mA) was used as the X-ray source. Thermogravimetric (TGA) and differential thermal (DTA) analysis of nano-GAZ samples before calcination were performed simultaneously on a Shimadzu DTG-60 thermogravimetric analyzer. 20 mg of samples was used in each experiment and the sample was heated in air with a heating rate of 10 °C/min. The IR spectra of the sample were measured using a Shimadzu FTIR-8700 spectrometer having a resolution of 2 cm^{-1}. The sample was mixed and ground thoroughly with KBr to have a mixture consisting of 0.5–1% complex oxide and 15 mg of this powder mixture was pressed (under a pressure of 4 t/cm^2) into a wafer of 16 mm in diameter.

Catalytic reactions were performed in a micro-catalytic reactor (o.d. 1/4 in.) using a single pass, steady-state plug flow mode. The catalysts were crushed and sieved to 0.250–0.425 mm before loading into the reactor. The temperature of the catalyst bed was controlled and monitored by a thermocouple that was in contact with the top layer of the catalyst bed. The reaction mixture was obtained by blending three channels of flow, i.e., O_2, pyridine/He (where helium was saturated with pyridine by bubbling helium through pyridine), and He as a diluent; each of these three streams was controlled by an independent mass flow controller. A typical reaction feed with a space velocity of 15,000 h^{-1} consisting of 540 ppm (in molar) of pyridine and 10 vol.% of O_2. The concentration of pyridine was measured using a Shimadzu 17A GC equipped with an FID detector and an Antek N-containing compound detector. The Antek detector was calibrated using a Shimadzu NOA7000 Chemiluminescence NO_x detector, which was also used in this study for analyzing NO_x formation during the decomposition of pyridine. N_2 concentration was analyzed on another GC (Shimadzu 17A) using 5A molecular sieve column and a TCD detector. The analysis of each stream coming out from the reactor at a certain temperature was taken after the reaction had reached steady state for 1 h. The conversion of pyridine was calculated based on the pyridine composition at the inlet and outlet of the reactor. N_2 and NO_x yields were calculated from the respective N_2 and NO_x concentration at the reaction exhaust as follows: N_2 yield = 2 × N_2 concentration in exhaust (ppm)/pyridine feed concentration (ppm). NO_x yield = NO_x concentration in exhaust (ppm)/pyridine feed concentration (ppm).

Catalytic activities of the nano-GAZ catalyst for SCR of NO in the presence of excess oxygen were also evaluated using the micro-catalytic reactor under a mode of steady-state plug flow. The total gas flow rate was 200 ml/min and 1.0 g of catalyst was packed in the reactor. The reaction mixture typically consisted of 1000 ppm of NO, 1000 ppm of C_3H_6, and 10 vol.% of O_2 (balanced in He). The concentration of C_3H_6, CO_2, and N_2O in the reaction exhaust was analyzed by a GC (Shimadzu GC-17A) equipped with a Porapak Q column and a TCD, and that of NO_x and O_2 was measured by a chemiluminescence NO_x/O_2 analyzer (Shimadzu NOA-7000).

3. Results and discussion

Fig. 1 shows TEM images characterizing the morphology and particle size of nano-GAZ material. Uniform nano-

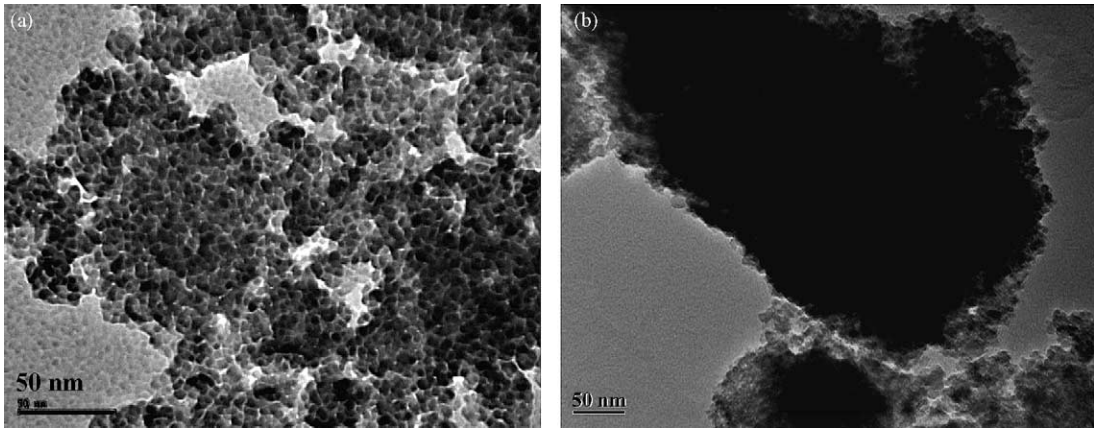

Fig. 1. TEM image of (a) nano-GAZ and (b) the contrasting sample prepared by precipitation (scale bar, 50 nm).

crystalline particles of size around 7–10 nm are obtained after calcination at 750 °C for 5 h. For comparison, the particle size of the contrasting complex-oxide sample prepared by precipitation is larger and irregular.

The spinel crystal structure of nano-GAZ solid solution is confirmed by XRD spectra and FTIR vibrational frequency spectra. The XRD patterns of nano-GAZ are consistent with that of the contrasting sample prepared by precipitation. All the diffraction peaks can be indexed to be a typical spinel structure [23]. Fig. 2 shows FTIR spectra characterizing the framework vibration of nano-GAZ as well as that of the contrasting sample prepared by precipitation. Since the characteristic IR vibrational frequencies are suitable for the identification of spinel phases, the four IR active vibrations, which are assigned according to the calculated vibrational frequencies of space group *Fd3m* of cubic spinel, are found to be at 690, 575, 518, and 227 cm^{-1}, respectively [24]. From an analysis of the IR spectra shown in Fig. 2, three active vibrational IR peaks of $\nu1$–$\nu3$ (670, 556, and 505 cm^{-1}) are present for the nano-GAZ catalyst and the contrasting sample prepared by precipitation. Although the observed vibrational frequencies have been shifted from the calculated ones, the observed frequencies are in excellent agreement with the literature reporting the observed frequencies for fully crystallized solid materials with spinel structure [25]. Due to the difference in particle size, nano-GAZ has a weaker vibrational IR band at around 505 cm^{-1} than the contrasting sample prepared by precipitation.

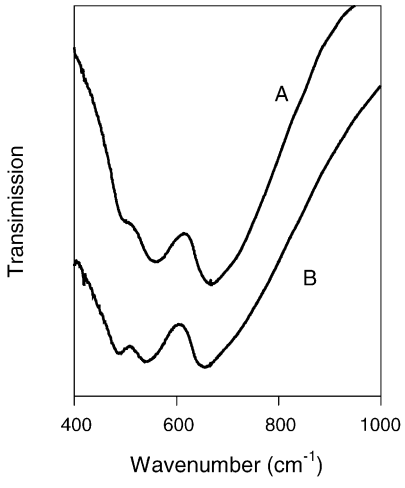

Fig. 2. FTIR spectra characterizing framework vibration of (A) nano-GAZ and (B) the contrasting sample prepared by precipitation.

The N_2 adsorption–desorption isotherms of nano-GAZ have a large H1-type hysteresis loop at P/P_0 around 0.45–0.75, which is related to the capillary condensation associated with large pore channels. Based on the isotherm desorption branch, a narrow Gaussian distribution peak at 38 Å is observed for nano-GAZ, suggesting that nano-GAZ has very uniform nanopore channels. For comparison, nano-GAZ has higher N_2 adsorption amount than the contrasting sample prepared by precipitation and the pore size of the contrasting sample is not uniform, indicating that the uniform pore size is formed only through hydrothermal synthesis. Since the nanoscaled pore structure of nano-GAZ is not as regularly arranged as that of mesoporous MS41 materials, such as MCM-41 or MCM-48 [17], the uniform pores of nano-GAZ are attributed to the uniform interstices of the nanocrystalline particles. The non-uniform pore size of the contrasting sample prepared by precipitation indicates the presence of non-uniform large particles. The surface area of nano-GAZ is 130.7 m^2/g, whereas it is only 72.3 m^2/g for the contrasting material prepared by precipitation.

Fig. 3 displays the TGA–DTA profiles of nano-GAZ before calcination. An endothermic DTA peak below 150 °C, which is accompanied by 15% weight loss, is attributed to the desorption of physically adsorbed water. A strong endothermic peak at around 200–280 °C, which is accompanied by a weight loss of about 50% of initial weight, is attributed to the dehydration of metal hydroxides. This strong endothermic peak is followed by a sharp exothermic peak at 290 °C, which is attributed to the solid reaction between zinc oxides, gallium oxides and aluminium oxides in the formation of crystallized spinel $ZnGaAlO_4$. Above

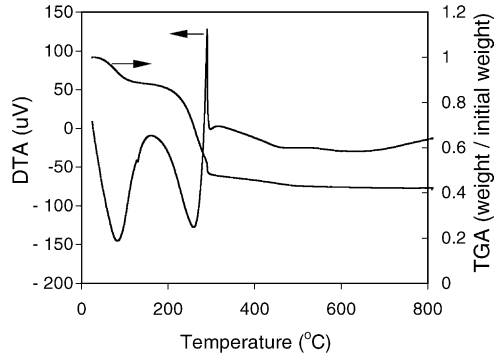

Fig. 3. DTA–TGA curves of nano-GAZ before calcination.

310 °C, the weight of spinel nano-GAZ is constant. The slight increase of the DTA signal above 700 °C may be attributed to the connecting growth among nanoparticles as the TEM image of nano-GAZ shows that its nanoparticles are not smooth and not clearly separated from each other.

Fig. 4 depicts the conversion of pyridine and the yield of NO_x at different reaction temperatures over the nano-GAZ catalyst and without the catalyst. For blank reaction without catalyst, the conversion of pyridine starts at temperature above 350 °C and reaches 100% combustion at 500 °C. Meanwhile, the formation of NO_x is found to be directly increased with the increase in the conversion of pyridine when the reaction temperature rises from 350 to 550 °C. Above 550 °C, more than 95% of NO_x yield is observed, indicating that most of pyridine is combusted in the gas phase reaction to NO_x, H_2O, and CO_2.

However, higher conversion is observed at lower temperature over the nano-GAZ catalyst than the blank reaction, showing that surface reaction increases the rate of pyridine combustion. From 300 to 400 °C, the conversion of pyridine increases with the increase of reaction temperature, with the formation of NO_x increasing simultaneously with the conversion of pyridine as pyridine is oxidized to NO_x, CO_2, and H_2O below 400 °C. Above 400 °C, the conversion of pyridine increases quickly to 100%, but interestingly, the yield of NO decreases to a very low level. At around 440–

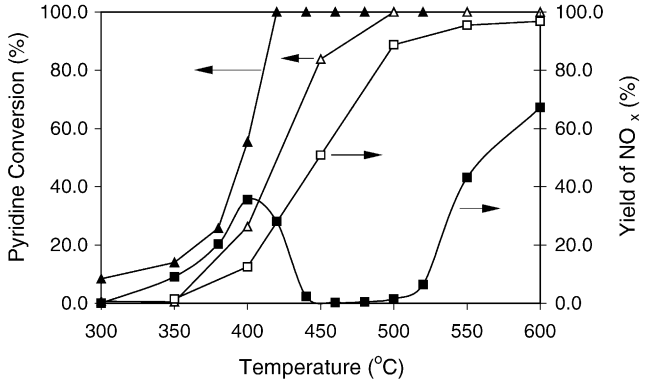

Fig. 4. Conversion of pyridine and yield of NO_x over nano-GAZ catalyst (solid symbol, ■ ▲) and under blank reaction (open symbol, □ △).

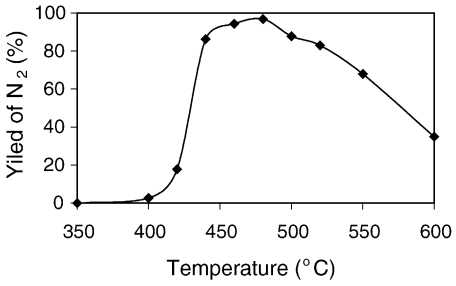

Fig. 5. Yield of N_2 for pyridine combustion over nano-GAZ catalyst.

500 °C, although pyridine is completely decomposed over nano-GAZ catalyst but the yield of NO is less than 5%. This interesting result may be explained by the fact that the NO formed during the oxidation of pyridine on the nano-GAZ catalyst surface could be reduced by hydrocarbon intermediate species produced during the oxidative decomposition of pyridine. Above 500 °C, the yield of NO_x increases significantly with the increase of reaction temperature. This may be explained as follows: as the oxidation of 540 ppm of pyridine was performed in this study in a reaction system containing 10 vol.% of oxygen, the hydrocarbon intermediates formed on the nano-GAZ catalyst surface competes intensively either for in situ reduction of NO_x or for direct oxidation to CO_2. At temperatures above 500 °C, the hydrocarbon intermediates seem to react preferably with oxygen rather than to reduce NO_x. This may be the reason why the formation of NO_x increases at temperatures higher than 500 °C.

Fig. 5 displays the yield of N_2 resulting from combustion of pyridine over nano-GAZ catalyst. It is important to note that the high yield of N_2 occurs at the optimal reaction temperature around 440–520 °C, indicating that most of the pyridine has been converted mainly to N_2. Below 420 °C, since the yield of N_2 is very low, the formation of NO_x increases with the increase of pyridine conversion. Above 520 °C, the yield of N_2 decreases with increasing reaction temperature, and is accompanied with the increase of NO_x formation (as shown in Fig. 4). This result confirms that, at the optimal reaction temperature window, NO_x produced from the decomposition of pyridine could be reduced in situ to N_2 on the surface of nano-GAZ catalyst. The formation of N_2O is lower than 3.0% at temperatures around 400–600 °C and N-balance analysis is found in the range of 94–104% based on pyridine, N_2, NO_x, and N_2O measurements.

Fig. 6 shows the formation of NO_x during the combustion of pyridine under different conditions. The contrasting Ga–Al–Zn complex oxide sample prepared by precipitation has higher NO formation than the blank reaction below 400 °C, showing that the combustion of pyridine is facilitated over the catalyst but the catalyst is not active for NO reduction at temperatures below 400 °C. Above 400 °C, the yield of NO_x is significantly lowered as compared with blank reaction, implying that some NO_x formed on this catalyst could be reduced to N_2 at higher temperatures. This is in good

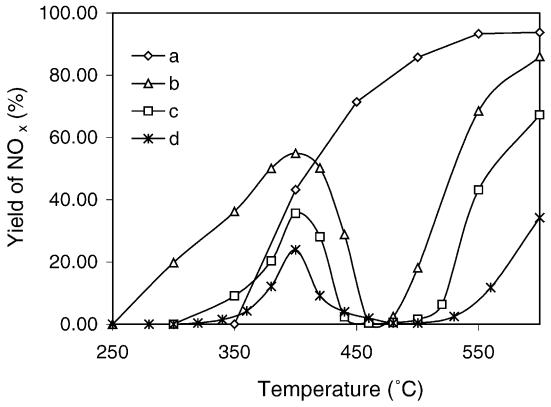

Fig. 6. Yield of NO_x produced during pyridine oxidation: (a) blank reaction, (b) Zn-Ga-Al complex oxides prepared by precipitation, (c) nano-GAZ catalyst, and (d) pyridine co-combustion with 1000 ppm of C_3H_8 over nano-GAZ catalyst.

agreement with literature that Ga–Al–Zn complex oxides have high activity for NO reduction by hydrocarbons at high temperatures [23]. For combustion of pyridine, the formation of NO over the surface of the catalyst could be reduced by the hydrocarbon species derived from the oxidative decomposition of pyridine before the NO_x species desorb from the catalyst surface. For nano-GAZ catalyst, the formation of NO_x is further suppressed at all temperature ranges as compared to the contrasting sample prepared by precipitation. The lower yield of NO_x over nano-GAZ catalyst is believed to be attributed to its higher surface area, which then provides more active sites for NO_x reduction. Fig. 6 also shows that, when pyridine is co-combusted with C_3H_8, the presence of C_3H_8 in the reaction stream further abates NO_x formation during oxidation of pyridine and most NO species could be reduced to N_2 at temperature regions of 440–550 °C. This result may be explained by the fact that, in the presence of C_3H_8, more hydrocarbon species are then available for NO reduction.

Fig. 7 shows the reactivity of nano-GAZ catalyst for SCR of NO with C_3H_6 in the presence of 10 vol.% of O_2 after the catalyst has been steamed at 750 °C for 40 h. At reaction temperatures below 460 °C, both NO and C_3H_6 conversions

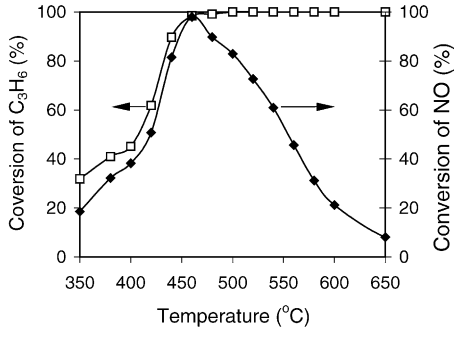

Fig. 7. Catalytic activity for SCR of NO with C_3H_6 in the presence of excess oxygen (reaction conditions: 1000 ppm of NO, 1000 ppm of C_3H_6, 10 vol.% of O_2, 1.0 g of catalyst, total flow rate = 200 mL/min).

increase simultaneously with the increase of reaction temperature, showing that a trace amount of C_3H_6 performs as an excellent reductant to selectively reduce NO in the presence of excess O_2. The maximum NO conversion reaches 97.8% at 460 °C. Above 500 °C, C_3H_6 is completely oxidized and the conversion of NO decreases due to the insufficient amount of hydrocarbon intermediates available on the catalyst surface for NO reduction. With a further increase of reaction temperature, the oxidation of hydrocarbon dominates the overall reaction, thus SCR of NO is further suppressed and the conversion of NO decreases to 10% at 650 °C. This reaction behavior of SCR-NO over nano-GAZ catalyst is similar to the variation of NO_x formation during the pyridine oxidation over nano-GAZ catalyst. This result indicates that the mechanism for the *in situ* reduction of NO_x by hydrocarbon intermediate species derived from the oxidative decomposition of pyridine is similar to the SCR of NO_x by hydrocarbons. Below 400 °C, since nano-GAZ catalyst is active for pyridine oxidization but less active for NO reduction, NO formation increases with the increase of pyridine conversion. Above 400 °C, NO_x formation decreases significantly since nano-GAZ catalyst facilitates the reduction of NO_x to N_2 with hydrocarbon intermediate species derived from the oxidative decomposition of pyridine. As both hydrocarbon intermediates and NO_x are produced from the pyridine oxidation on the catalyst surface, there is a very high likelihood that they are in close interaction; hence, hydrocarbon intermediates reduce NO_x to N_2 before they desorb to the gas phase. The nano-GAZ catalyst shows better performance for the *in situ* reduction of NO_x during pyridine oxidation than the SCR-NO reaction with externally-introduced hydrocarbon in the presence of excess oxygen. Furthermore, it is important to mention here that the nano-GAZ catalyst has very high hydrothermal stability. This is because nano-GAZ catalyst was still very active for SCR of NO_x in the presence of excess oxygen although it has been steamed at 750 °C for 40 h before being used in the reaction. For a comparison, zeolite-based catalysts – when they are subjected to the same hydrothermal treatment conditions – are seriously deactivated for SCR-NO [20].

Since the conventional three-way catalyst (TWC) is known to be inefficient for the removal of NO_x under a lean-burn condition, this limits its application as an environmental catalyst for new-generation vehicles operated with lean-burn engines. The superior performance of nano-GAZ catalyst exhibits great potential for simultaneous degradation of N-containing polycyclic aromatic compound and abatement of NO_x emission in the presence of excess oxygen. It is worth noting that the optimal temperature region of nano-GAZ is also a suitable operating condition for an in-use catalytic converter. Hence, coupling our nano-GAZ catalyst in the catalytic converter of a new-generation vehicle may enable on-road traffic to be more environmental friendly as nano-GAZ catalyst can perform both deNOx and deNPAC satisfactorily.

4. Conclusion

Nano-GAZ catalyst, obtained by hydrothermal synthesis, has particles sizes around 5–10 nm, spinel crystal structure and larger surface areas as compared with the contrasting sample prepared by precipitation. Nano-GAZ catalyst not only has good activity for combustion of pyridine but also has good control for limiting NO_x formation from oxidative decomposition of pyridine. The optimal reaction temperature for complete conversion of pyridine and low NO_x formation yield (<5%) is observed at 440–500 °C. Nano-GAZ catalyst performs well as a dual-function catalyst in both oxidizing NPACs and controlling NO_x formation.

Acknowledgment

This work has been generously supported by the National Science and Technology Board of Singapore (R-297-000-093-303) and the National University of Singapore (R-297-000-093-112).

References

[1] D. Schuetzle, M.C. Paputa-peck, R.S. Marano, T.L. Riley, C.V. Hampton, T.J. Prater, L.M. Skewes, T.E. Jensen, P.H. Ruehle, L.C. Bosch, W.P. Duncan, Anal. Chem. 55 (1983) 1946.
[2] H.U.R. Memon, K.D. Bartle, J.M. Taylor, A. Williams, Intern. J. Ener. Res. 24 (2000) 1141.
[3] Z.R. Ismagilov, M.A. Kerzhentsev, V.I. Besedin, T.L. Susharina, React. Kinet. Catal. Lett. 23 (1983) 43.
[4] Z.R. Ismagilov, M.A. Kerzhentsev, V.I. Besedin, T.L. Susharina, React. Kinet. Catal. Lett. 23 (1983) 49.
[5] Z.R. Ismagilov, M.A. Kerzhentsev, Catal. Rev. Sci. Eng. 32 (1990) 51.
[6] S. Sato, Y. Yuu, H. Yahiro, N. Mizuno, M. Iwamoto, Appl. Catal. 70 (1991) L1.
[7] Y. Traa, B. Burger, J. Weitkamp, Microporous Mesoporous Mater. 30 (1999) 3.
[8] X.Y. Chen, S.C. Shen, H.H. Chen, S. Kawi, J. Catal. 221 (2004) 137.
[9] R. Burch, P.J. Millington, Appl. Catal. B: Environ. 2 (1993) 2.
[10] T. Tabata, M. Kokitsu, H. Ohtsuka, O. Okada, L.M.F. Sabatino, G. Bellussi, Catal. Today 27 (1996) 91.
[11] W.E.J. van Kooten, B. Liang, H.C. Krijnsen, O.L. Oudshoon, H.P.A. Calis, Appl. Catal. B: Environ. 21 (1999) 203.
[12] D.K. Captain, K.L. Robert, M.D. Amiridis, Catal. Today 42 (1998) 93.
[13] S.C. Shen, S. Kawi, Appl. Catal. B: Environ. 45 (2003) 63–76.
[14] I.V. Yentekakis, R.M. Lambert, M. Konsolakis, V. Kiousis, Appl. Catal. B: Environ. 18 (1998) 293.
[15] R. Burch, J.P. Breen, F.C. Meunier, Appl. Catal. B: Environ. 39 (2002) 283.
[16] Y. Kintaichi, H. Hamada, M. Tabata, M. Sasaki, T. Ito, Catal. Lett. 6 (1990) 239.
[17] J.R. Gonzalez-Velasco, M.A. Gutierrez-Ortiz, J.L. Marc, J.A. Botas, M. Pilar Gonzalez-Marcos, G. Blanchard, Appl. Catal. B: Environ. 22 (1999) 167.
[18] M. Haneda, Y. Kintaichi, H. Hamada, Appl. Catal. B: Environ. 20 (1999) 289.
[19] Y. Okimura, H. Yokoi, K. Ohbayashi, K. Shimizu, A. Satsuma, T. Hattori, Catal. Lett. 52 (1998) 157.
[20] S.C. Shen, K. Hidajat, L.E. Yu, S. Kawi, Adv. Mater. 16 (2004) 541.
[21] M.D. Fokema, J.Y. Ying, Catal. Rev. Sci. Eng. 43 (2001) 1.
[22] P.T. Tanev, L.T. Vlaev, J. Colloid Interface Sci. 160 (1993) 160.
[23] Y. Okimura, H. Yokoi, K. Ohbayashi, K. Shimizu, A. Satsuma, T. Hattori, Catal. Lett. 52 (1998) 157.
[24] J. Preudhomme, P. Tarte, Spectrochim. Acta 27A (1971) 961.
[25] C. Kinle, C. Schinzer, J. Lentmaier, O. Schaal, S. Kemmler-Sack, Mater. Chem. Phys. 49 (1997) 211.